# *In vivo* carbon nanotube-enhanced non-invasive photoacoustic mapping of the sentinel lymph node

**Manojit Pramanik[1], Kwang Hyun Song[1], Magdalena Swierczewska[2], Danielle Green[2], Balaji Sitharaman[2] and Lihong V Wang[1]**

[1] Department of Biomedical Engineering, Optical Imaging Laboratory, Washington University, St Louis, MO 63130, USA
[2] Department of Biomedical Engineering, State University of New York, Stony Brook, NY 11794, USA

E-mail: lhwang@biomed.wustl.edu (PA) and balaji.sitharaman@stonybrook.edu (CNT)

## Abstract

Sentinel lymph node biopsy (SLNB), a less invasive alternative to axillary lymph node dissection (ALND), has become the standard of care for patients with clinically node-negative breast cancer. In SLNB, lymphatic mapping with radio-labeled sulfur colloid and/or blue dye helps identify the sentinel lymph node (SLN), which is most likely to contain metastatic breast cancer. Even though SLNB, using both methylene blue and radioactive tracers, has a high identification rate, it still relies on an invasive surgical procedure, with associated morbidity. In this study, we have demonstrated a non-invasive single-walled carbon nanotube (SWNT)-enhanced photoacoustic (PA) identification of SLN in a rat model. We have successfully imaged the SLN *in vivo* by PA imaging (793 nm laser source, 5 MHz ultrasonic detector) with high contrast-to-noise ratio (=89) and good resolution (∼500 $\mu$m). The SWNTs also show a wideband optical absorption, generating PA signals over an excitation wavelength range of 740–820 nm. Thus, by varying the incident light wavelength to the near infrared region, where biological tissues (hemoglobin, tissue pigments, lipids and water) show low light absorption, the imaging depth is maximized. In the future, functionalization of the SWNTs with targeting groups should allow the molecular imaging of breast cancer.

(Some figures in this article are in colour only in the electronic version)

## 1. Introduction

For the majority of invasive breast cancers, the surgical removal of primary breast tumor and level I and level II axillary lymph node dissections (ALND) are widely performed (NIH Consensus Statement 1990). However, common side effects after ALND include

upper-extremity lymphedema, arm numbness, impaired shoulder mobility, arm weakness and infections in the breast, chest or arm (Swenson *et al* 2002). A less invasive, more accurate alternative to ALND is sentinel lymph node biopsy (SLNB). For patients with clinically node-negative breast cancer, SLNB has rapidly become the standard of care (Krag *et al* 1998, McMasters *et al* 2000). The concept of a SLNB assumes that the primary draining or sentinel node will be the first to contain metastases. The hypothesis is that both the mammary gland and overlying skin share a common lymphatic pathway to the same axillary sentinel node. Therefore, intradermal injection of blue dye will lead to the accumulation of the dye in the sentinel lymph nodes (Borgstein *et al* 1997). In this surgery, a special blue dye and/or a radioactive substance is first injected into the breast to determine which lymph nodes are the first to receive drainage from the breast. These nodes are potentially the first to be invaded by cancer cells. One to three sentinel nodes are usually removed and tested for cancer. If cancerous, then all the lymph nodes are removed. This surgery has fewer complications than axillary node dissection, but the physicians performing the procedure must have special training. The identification rate and sensitivity of this technique are less than 95%, even in experienced hands (Krag *et al* 1998, McMasters *et al* 2000, Ung 2004). Furthermore, the complications associated with the SLNB procedure include seroma formation, lymphedema, sensory nerve injury and limitation in the range of motion (Purushotham *et al* 2005). These limitations of SLNB strongly suggest that alternative strategies to stage the axilla should be explored.

Axillary ultrasound (AUS) has been proposed as a potential non-invasive technique for identifying axillary metastases (Krishnamurthy *et al* 2002, Deurloo *et al* 2003, Brancato *et al* 2004). AUS can visualize the lymph node's size, shape and contour, as well as changes in cortical morphology and texture that appear to be associated with the presence of axillary metastases. However, the ability of AUS alone to stage the axilla accurately is limited because the sonographic signs of metastatic disease may overlap with those of benign reactive changes. On the other hand, *in vivo* identification of a sentinel lymph node (SLN) using photoacoustic (PA) imaging would allow non-invasive axillary staging, in conjunction with either percutaneous fine-needle aspiration biopsy (FNAB) or other emerging molecular techniques.

Photoacoustic tomography (PAT) (Hoelen *et al* 1998, Ku and Wang 2005, Ku *et al* 2005, Zhang *et al* 2006, Song and Wang 2007, Song *et al* 2008) that combines the advantages of optical absorption contrast with ultrasonic spatial resolution has emerged as an excellent technique for non-invasive imaging of biological tissues, offering high spatial resolution and high soft tissue contrast. *In vivo* PA imaging of SLN in a rat model was also reported using methylene blue (Song *et al* 2008). However, methylene blue does not permit molecular imaging. Recently, single-walled carbon nanotube (SWNT)-based contrast agents have shown a promise for a variety of imaging techniques. The prospect of SWNTs as a contrast agent for PA imaging was also reported (Pramanik *et al* 2009). In this study, we exploited the intrinsic optical absorbance (Hughes *et al* 2007, Berciaud *et al* 2007) of carbon nanotubes to develop them as contrast agents, and used them to perform non-invasive imaging of SLN in a rat model *in vivo*.

## 2. Methods and materials

### 2.1. Photoacoustic imaging

A reflection-mode PA imaging system (Song and Wang 2007) was used to get the PA spectroscopy of the SWNTs. A tunable Ti:sapphire laser (LT-2211 A, LOTIS TII) pumped

by Q-switched Nd:YAG (LS-2137, LOTIS II) laser was the light source, providing <15 ns pulse duration and a 10 Hz pulse repetition rate. A dark-field ring-shaped illumination was used (Maslov *et al* 2005). The light energy on the sample surface was controlled to conform to the American National Standards Institute (ANSI) standard for maximum permissible exposure (MPE) (ANSI 2000). A 3.5 MHz/5 MHz central frequency, spherically focused (4.95 cm/2.54 cm focus length, 1.91 cm diameter active area element and 70%/72% bandwidth) ultrasonic transducer (V380/V308, Panametrics-NDT) was used to acquire the generated PA signals. The signal was then amplified by a low-noise amplifier (5072PR, Panametrics-NDT) and recorded using a digital oscilloscope (TDS 5054, Tektronix) with a 50 mega-sampling rate. PA signal fluctuations due to pulse-to-pulse energy variation were compensated by signals from a photodiode (DET110, Thorlabs), which sampled the energy of each laser pulse.

A linear translation stage (XY-6060, Danaher Motion) was used for raster scanning to obtain three-dimensional (3D) PA data. A computer controlled the stage and synchronized it with the data acquisition. To shorten the data acquisition time, a continuous scan was used without signal averaging. An A-line (A-scan) was the PA signal obtained along the depth direction at a single point. Multiple A-lines (acquired by a one-dimensional (1D) scan) gave a two-dimensional (2D) B-scan. A 3D image was acquired with a 2D scan. A 1D depth-resolved image was obtained by multiplying the time axis of the initial A-scan (resolved in time along the depth direction) by the speed of sound in soft tissue ($\sim$1500 m s$^{-1}$).

The scanning time depends on the laser pulse repetition rate (PRR), the scanning step size and the field of view (FOV). Typical values are a scanning step size for a 1D scan = 0.1 mm, for a 2D scan = 0.2 mm, a laser PRR = 10 Hz and a FOV = 20 mm × 20 mm. The acquisition time = $\sim$25 s for a B-scan and = $\sim$42 min for a 3D image. The transducer was located inside a water container with an opening of 5 cm × 5 cm at the bottom, sealed with a thin, clear membrane. The object was placed under the membrane, and ultrasonic gel was used for coupling the sound.

### 2.2. SWNTs synthesis

Iron (Fe) was coated onto a silicon wafer using the diblock copolymer template method (Fu *et al* 2004). SWNTs were synthesized using the carbon vapor deposition (CVD) method with Fe as the metal catalyst (Easy Tube 2000, First Nano). The wafer was placed into a 3 inch quartz reaction chamber that was heated with Ar at 900 °C, hydrogen gas was added for 2 min and methane was fed into the reactor for 20 min to grow SWNTs over the Fe catalyst. The SWNTs were further dispersed in 1 wt% Pluronic® F127 surfactant (1 g of surfactant in 100 g of deionized water) at the appropriate concentration and sonicated rigorously to obtain a homogeneous dispersion. To visualize the SWNT structure, transmission electron microscopy (TEM) was performed (Tecnai12 BioTwinG2, FEI, Hillsboro, OR) at 80 kV on SWNT samples mounted on a 400 mesh copper grid with formvar coating. High resolution TEM (hrTEM) (JEOL 2000 FX) was also performed at 200 kV for SWNT samples mounted on a copper grid that was coated with amorphous carbon-holey film. In addition, atomic force microscopy (AFM) was also performed (MFD-3D-BIO, Asylum Research, Santa Barbara, CA). A Raman spectrum of the SWNTs was also taken at 633 nm (LabRam Aramis, Horiba JvonYvon).

### 2.3. Animal and drug information

Guidelines on the care and the use of laboratory animals at Washington University in St Louis were followed for all animal experiments. Adult Sprague Dawley rats with various
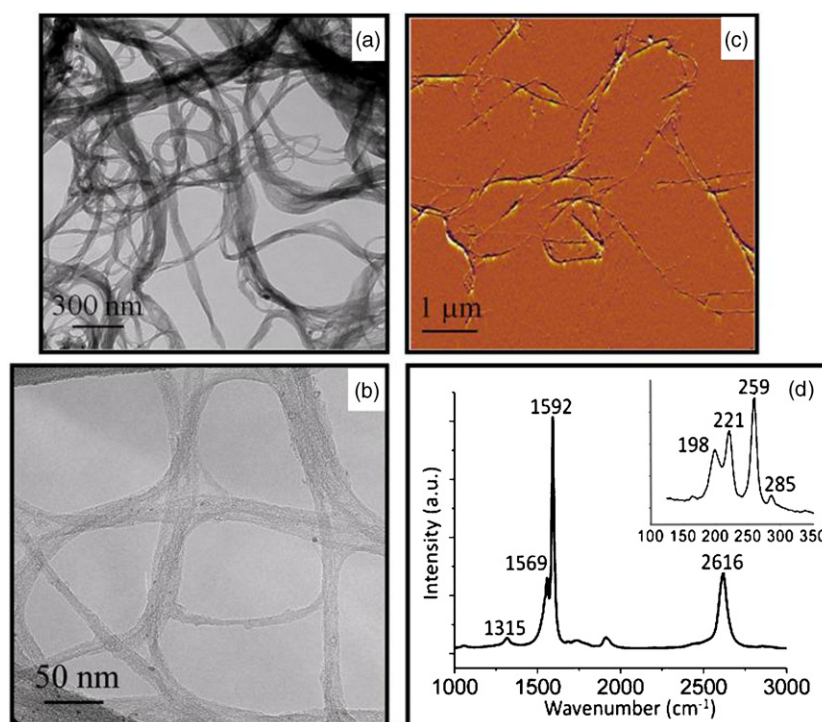
**Figure 1.** SWNT characterization. (a) TEM and (b) hrTEM image of the SWNTs produced by the Fe catalyst. (c) AFM image of the SWNTs produced by the Fe catalyst, confirming the nanotube diameter of 2 nm. (d) A Raman spectrum of the SWNT obtained at 633 nm. The G band is at 1592 cm$^{-1}$, while the D band is found at 1315 cm$^{-1}$. The radial breathing modes occur between 100 and 350 cm$^{-1}$ (see the inset).

body weights (250–350 g) were used for the experiments. Initial anesthetization of the rat was done using a mixture of ketamine (85 mg kg$^{-1}$) and xylazine (15 mg kg$^{-1}$). The hair on the region of interest of the rat was gently removed before imaging, using a commercial hair-removal lotion. Intradermal injection of 0.075 ml of 0.5 mg ml$^{-1}$ SWNTs was performed on a left/right forepaw pad, depending on which side was imaged. PA images were acquired after the administration of SWNTs. During the image acquisition, anesthesia was maintained using vaporized isoflurane (1 L min$^{-1}$ oxygen and 0.75% isoflurane, Euthanex Corp.), and a pulse oximeter (NONIN Medical Inc., 8600 V) was used to monitor the vitals. If needed, 8 ml of 0.9% saline was administered to the rat for hydration. After image acquisition, the animal was euthanized by pentobarbital overdose.

## 3. Results and discussions

### 3.1. Characterization of SWNTs

Figure 1 shows the TEM, hrTEM and Raman spectroscopy of the synthesized SWNTs used in this study. These images were used to characterize the SWNTs. Figures 1(a) and (b) show low-resolution bright field TEM and the hrTEM images of the SWNTs, respectively. These two figures confirm the growth of SWNTs with an approximate diameter of 2 nm. Figure 1(c) shows an AFM image, which confirms that the SWNT diameters were consistent with the
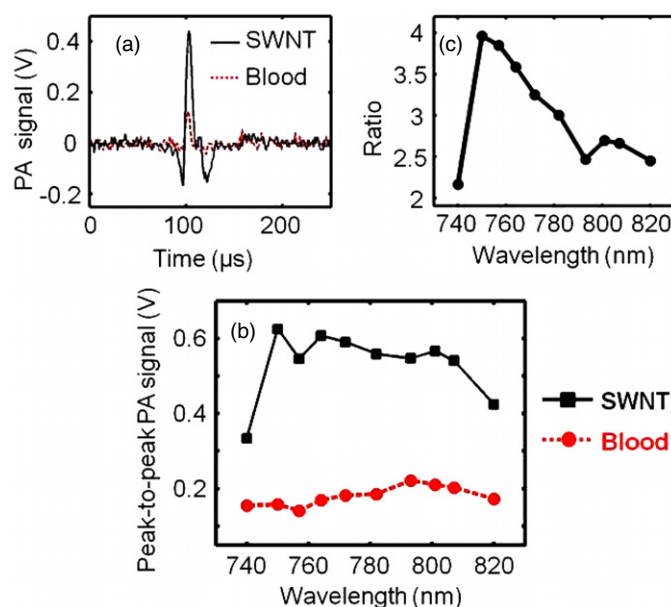
**Figure 2.** (a) PA signals generated from a tygon tube (I.D. 250 $\mu$m, O.D. 500 $\mu$m) filled with SWNTs (0.25 mg ml$^{-1}$) and rat blood. The excitation optical wavelength is 764 nm. (b) PA spectra of SWNTs and blood over a 740–820 nm range of NIR wavelengths. (c) Ratio of the peak-to-peak PA signal amplitudes generated from SWNTs to those generated from blood.

diameters observed in the hrTEM image. Figure 1(d) shows the Raman spectrum of the SWNTs at 633 nm. The Raman spectrum shows the G band at 1592 cm$^{-1}$ and the D band at 1315 cm$^{-1}$. The G band is a peak specific to graphene, while the D band indicates defects on the graphene sheet. The low D band to G band ratio signifies few defects in the SWNT sample. The radial breathing modes, which occur in the presence of small diameter tubes of a single graphene layer, can be viewed within the inset, and further confirm that these samples were SWNTs (Dresselhaus *et al* 2005).

### 3.2. Photoacoustic spectroscopy of SWNTs

Blood is a dominant optical absorber in the human body and produces strong PA signals. Therefore, the PA signal from SWNTs was compared with that from blood to show that SWNTs are capable of generating PA signals comparable to or stronger than that of a known absorber in the body in the near infrared (NIR) wavelength window. Figure 2(a) shows the PA signals obtained from a tygon tube (I.D. 250 $\mu$m, O.D. 500 $\mu$m) filled with SWNTs (0.25 mg ml$^{-1}$) and rat blood. The laser was tuned to 764 nm wavelength. At this excitation wavelength, the peak-to-peak PA signal amplitude obtained from SWNTs was ~600 mV, compared to a ~170 mV peak-to-peak PA signal amplitude from blood alone. Figure 2(b) shows the PA spectrum (peak-to-peak PA signal amplitude versus excitation light wavelength) of the SWNTs (in black) for an excitation wavelength range of 740–820 nm. The PA spectrum of rat blood (in red) is also shown in the same figure. It is evident that the PA signal obtained from SWNTs is much stronger than that of blood over the entire wavelength range. Therefore, one can choose a specific light wavelength for imaging within a broad range. Figure 2(c) plots the ratio of the peak-to-peak PA signal amplitude of SWNTs to that of blood between
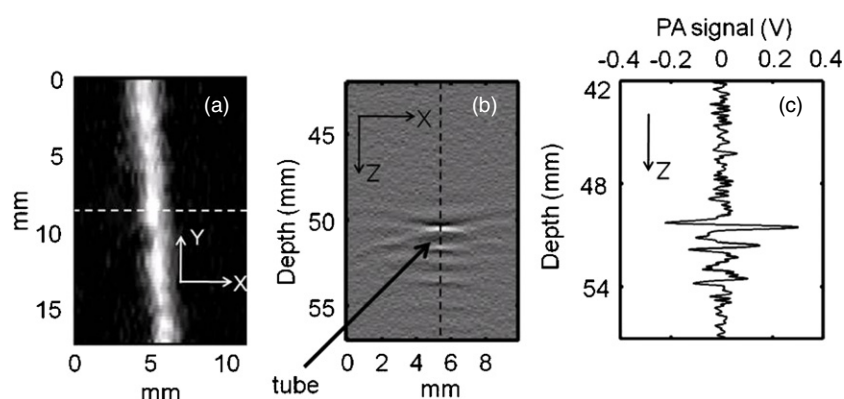
**Figure 3.** (a) Maximum amplitude projection (MAP) image of a tube (Silastic® laboratory tubing, Dow Corning Corp., with 1.47 mm I.D.) filled with SWNTs (1 mg ml$^{-1}$) placed inside chicken breast tissue. The tube was placed 20 mm below the top surface of the tissue. The PA image clearly shows the tube, with a CNR of 25. (b) PA B-scan image along the dotted line in (a), with the bright spot showing the PA signal originating from the tube filled with SWNTs. (c) Photoacoustic A-line along the dotted line in (b).

740 and 820 nm. The PA signal from the tygon tube filled with SWNTs is more than four times stronger than that from blood at 750 nm. Over the entire 740–820 nm window, the PA signal from SWNTs is more than two times stronger than that from blood. Due to the weak blood absorption, the NIR window is well known for providing deep tissue PA imaging at the expense of blood contrast. The strong PA signal from SWNTs in the NIR region implies that they could be used as contrast agents to boost the signal strength for PA imaging in this region.

### 3.3. Deep tissue imaging

The sensitivity of the PA imaging system was determined from chicken tissue phantom experiments, used to mimic human breast tissue (Song *et al* 2008). The light source was tuned to 793 nm wavelength. A tube (Silastic® laboratory tubing, Dow Corning Corp.) with 1.47 mm I.D. was placed between two layers of chicken breast tissue. The tube was filled with 1 mg ml$^{-1}$ SWNTs. The thickness of the tissue layer on top of the tube was ∼20 mm. Figure 3(a) shows the maximum amplitude projection (MAP) (Zhang *et al* 2006) image of the tube. The tube is clearly seen in the image, with a high contrast-to-noise ratio (CNR) of 25. Figure 3(b) shows the B-scan PA image (along the dotted line in figure 3(a)). The bright spot in the B-scan represents the PA signal generated from the tube filled with SWNTs. Figure 3(c) shows the A-line PA signal (along the dotted line in figure 3(b)), clearly showing the strong PA signal from the tube filled with SWNTs compared to the weak signal from the surrounding chicken breast tissue. These results prove that use of SWNTs as a contrast agent enables tissue imaging more than 20 mm deep. For human studies, the depth of imaging is very important, as the mean depth of SLNs is $12 \pm 5$ mm (distance from the skin surface to the top surface of SLN) (Margenthaler 2007). Therefore, the ability to image more than 20 mm deep with high CNR and high resolution is a key for mapping SLN non-invasively.

### 3.4. Sentinel lymph node imaging non-invasively in a rat in vivo

Adult Sprague Dawley rats with various body weights (250–350 g) were used for the experiments. The hair on the axillary region of the rat was removed and a PA image was
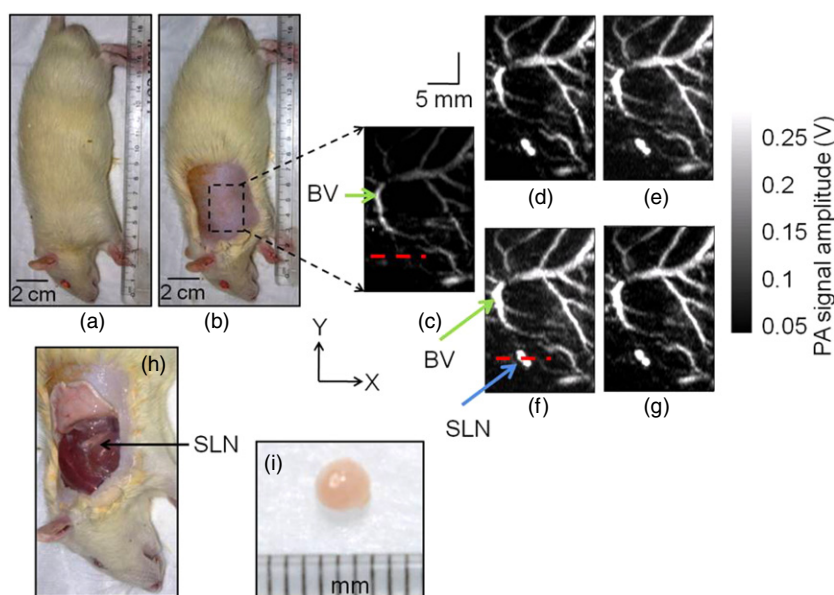
**Figure 4.** Non-invasive *in vivo* PA images (MAP) of the SLN in a rat. For all PA images, the laser was tuned to 793 nm wavelength. (a) Photograph of the rat. (b) Photograph of the rat after the hair was removed from the scanning region before taking the PA images. The scanning region is marked with a black dotted square. (c) Control PA image acquired before SWNT injection. Bright parts represent optical absorption, here, from blood vessels (BV). (d) PA image (MAP) acquired immediately after the SWNT injection. (e) 30 min post-injection PA image. (f) 55 min post-injection PA image. (g) 85 min post-injection PA image. Blood vessel (BV) and sentinel lymph node (SLN) are marked with arrows, and the SLN is visible in all images except the control image. (h) Photograph of the rat with the skin removed after PA imaging. (i) The excised lymph node. For (c)–(g): FOV = 25 mm × 30 mm, step size along the *X* direction = 0.2 mm, step size along the *Y* direction = 0.4 mm, total scan time = ∼23 min. No signal averaging was used. Only a FOV of 16 mm × 24 mm is shown.

taken. This image was a control image for comparison with future images. An intradermal injection of 0.075 ml of 0.5 mg ml$^{-1}$ SWNTs was performed on the forepaw pad. Four PA images were acquired at intervals of 25–30 min after the SWNTs injection. For all the PA images, the following parameters were used: FOV = 25 mm × 30 mm, step size along the *X* direction = 0.2 mm, step size along the *Y* direction = 0.4 mm and total scan time = ∼23 min. Please note that no signal averaging was done for any of these images. The images shown here are cropped to a FOV of 16 mm × 24 mm, since the outside region was not of interest.

Figure 4(a) shows a representative digital photograph of a rat taken prior to image acquisition, and figure 4(b) shows the shaved axillary surface where the PA imaging was performed. Before the SWNT injection, a PA control image was obtained, which is shown in the form of a MAP (Zhang *et al* 2006) in figure 4(c). The vasculature near an axial node (one blood vessel is marked as BV) was clearly imaged, with a high CNR of ∼79 and good resolution of ∼500 μm. Note that no lymph nodes are visible in the control image, since there is no intrinsic optical absorption in lymph nodes to produce any PA signal to image. Figure 4(d) shows the PA image (MAP) of the same area immediately after the SWNTs were injected, approximately 30 min after the control image was taken. Figures 4(e)–(g) are the post-injection PA images (MAP) of the same area 30, 55, and 85 min after the SWNTs injection. The SLN
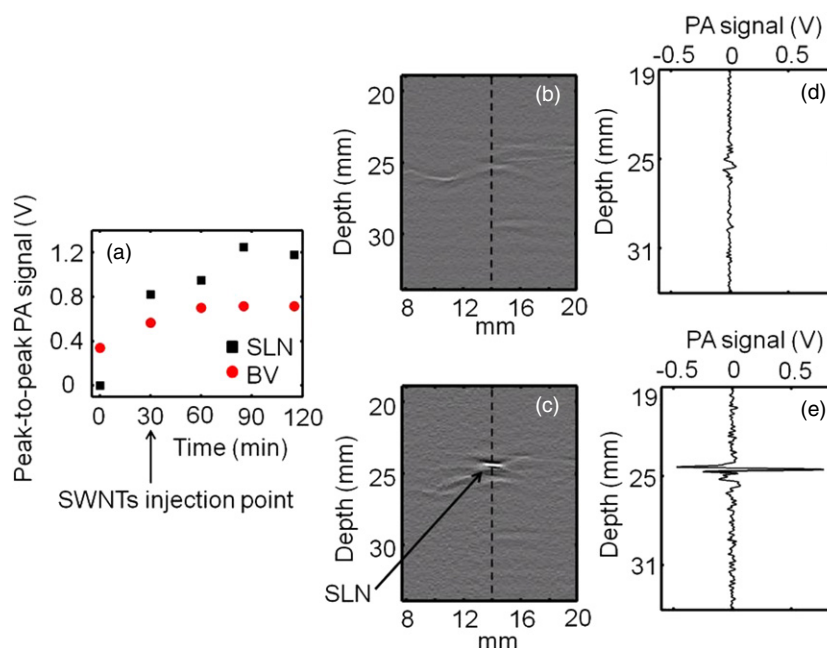
**Figure 5.** (a) Peak-to-peak PA signal amplitude obtained from SLN and blood vessel (BV) over time. The SWNTs were injected 30 min after the control scan. (b) PA B-scan image corresponding to the dotted line in (c), the control image. (c) PA B-scan image corresponding to the dotted line in (f), image showing the SLN. The bright spot represents the PA signal generated from the SLN. (d) A-line PA signal corresponding to the dotted line in (b). (e) A-line PA signal corresponding to the dotted line in (c), showing the strong PA signal generated from the SLN.

appears at the left lower quadrant, marked as SLN in figure 4(f), and is clearly visible in all the post-injection PA images (figures 4(d)–(g)). The images show high CNRs (74 in figure 4(d), 67 in figure 4(e), 84 in figure 4(f) and 89 in figure 4(g)). The contrast of the SLN to the surrounding blood vessel was up to 1.8 (ratio of the peak-to-peak PA signal amplitude obtained from SLN and BV) after SWNT injection. The signal amplitude of the surrounding blood vessels was also increased by up to ∼124% compared to that in the control image (94% in figure 4(d), 110% in figure 4(e), 124% in figure 4(f) and 105% in figure 4(g)), although the CNR remained almost the same. This increase in signal amplitude suggests that the SWNTs have traveled into the blood stream and the nearby tissues boosting the blood vessel signal as well as the background signal. Figure 4(h) is a digital photograph of the same rat with the skin removed after the completion of the PA imaging. Figure 4(i) is a digital photograph of the SLN removed from the rat (arrow in figure 4(i)). The photograph shows the SLN size to be 2 to 3 mm, matching the size obtained from PA images (figures 4(d)–(g)).

Figure 5(a) shows the uptake kinetics of the SWNTs. An increased PA signal was observed in both blood vessels and SLN during the first 30 min post-injection, with the SLN showing a greater increase than blood vessels at all time points. Subsequently, the PA signal in the blood reached a plateau while the PA signal in the SLN kept increasing. These results further corroborate the imaging data presented in figure 4, where increases in signal intensities were observed post-injection from both SLN and BV, but the intensity from SLN was stronger compared to the nearby blood vessels. The stronger signal is due to the strong light absorption of SWNTs compared to blood and to the greater accumulation of SWNTs in

the lymph node than in the surrounding blood vessels. Figures 5(b) and (c) show the B-scan PA images corresponding to the dotted lines marked in figures 4(c) and (f), respectively. The bright spot in figure 5(c) represents the strong PA signal from the SLN, which is not present in the pre-injection B-scan (Figure 5(b)). Figures 5(d) and (e) show the A-line PA signals corresponding to the dotted lines in figures 5(b) and (c), respectively. The strong PA signal obtained from the SLN is clearly seen in figure 5(e), whereas there is no such signal in the control image (figure 5(d)). We used a 0.5 mg ml$^{-1}$ concentration of SWNTs for our *in vivo* study (the average molecular weight of SWNTs is $\sim$10$^6$ Da or g mol$^{-1}$; 0.5 mg ml$^{-1}$ = 0.5 mg ml$^{-1}$/10$^6$ g ml$^{-1}$ = 500 nM). However, that choice does not limit the use of SWNTs at other lower concentrations (De La Zerda *et al* 2008). Our system is capable of detecting SWNTs on the order of nM concentration (Pramanik *et al* 2009).

Our results show that non-invasive *in vivo* PA imaging for SLN identification with the use of SWNTs as a contrast agent is highly feasible in a small animal model. Moreover, the PA imaging technique used here to image rat SLN can easily be translated to humans. Although SLN mapping using different contrast agents, e.g., carbon nanotubes, gold nanocages, gold nanorods and methylene blue dye, has been done successfully, we believe SWNTs have many advantages over the other materials. The broad absorption spectrum of SWNTs will provide us a wide range of light wavelengths for imaging. Most of the other contrast agents have narrow absorption spectra, restricting their use to a particular wavelength. SWNTs also show good efficacy as contrast agents for thermoacoustic imaging (Pramanik *et al* 2009). In the future, thermoacoustic tomography can also be combined with the PA imaging system for SLN mapping. Targeted SWNTs could also be used for more specific identification. Our previous PA studies demonstrated that SWNTs produce a PA signal at concentrations as low as 0.1 mg ml$^{-1}$ (Pramanik *et al* 2009). Using a 0.5 mg ml$^{-1}$ concentration of SWNTs, we have obtained very high CNR sentinel lymph node images (CNR = $\sim$90); thus, it can be inferred that we could detect SWNTs at concentrations as low as 0.01 mg ml$^{-1}$. Assuming that the SWNTs have an average diameter of 2 nm and average length of 1 $\mu$m, there should be $\sim$10$^5$ carbon atoms in one SWNT, as derived by Yamamoto *et al* 2005, and a SWNT has a molecular weight of $\sim$1.2 $\times$ 10$^6$ g mol$^{-1}$. Using these values, SWNTs should act as contrast agents in human blood at concentrations as low as 8 nM (0.1/1.2 $\times$ 10$^6$). SWNTs can also be functionalized in order to target specific tissues and to increase the SWNTs blood circulation time. This would prevent the SWNTs from being diluted in the human bloodstream for periods long enough to perform PA imaging.

Currently, this imaging system is limited by its slow scanning speed. Employing a higher pulse-repetition-frequency laser and an ultrasound array system could accelerate acquisition, potentially allowing real-time PA imaging (Yin *et al* 2004, Zeng *et al* 2004, Yang *et al* 2005). The *in vivo* biocompatibility of SWNTs needs to be thoroughly examined before its translation for clinical use. Nevertheless, since SLN identification by PA imaging is totally non-invasive and safe, it shows potential future clinical applications without the limitations of current invasive and minimally invasive techniques.

## 4. Conclusions

We have shown that the PA signal from SWNTs is stronger than that of blood over the NIR wavelength window (740–820 nm) and demonstrated a non-invasive SWNT-enhanced PA identification of SLN in a rat model *in vivo* with a high contrast-to-noise ratio (CNR = 89) and good resolution ($\sim$500 $\mu$m). We have also shown the possibility of deep tissue imaging (20 mm deep) using SWNTs as a contrast agent. Our results suggest that this technology could be a useful pre-clinical and possibly clinical tool to identify SLNs non-invasively

*in vivo*. In the future, the identification rate of node-negative breast cancer could be improved by functionalization of the SWNTs with targeting groups.

## Acknowledgments

## References

ANSI 2000 American National Standard for Safe Use of Lasers *ANSI Standard Z136.1*

Berciaud S, Cognet L, Poulin P, Weisman R B and Lounis B 2007 Absorption spectroscopy of individual single-walled carbon nanotubes *Nano Lett.* **7** 1203–7

Borgstein P J, Meijer S and Pijpers R 1997 Intradermal blue dye to identify sentinel lymph-node in breast cancer *Lancet* **349** 1668–9

Brancato B *et al* 2004 Role of ultrasound-guided fine needle cytology of axillary lymph nodes in breast carcinoma staging *Radiol. Med. (Torino)* **108** 345–55

De La Zerda A *et al* 2008 Carbon nanotubes as photoacoustic molecular imaging agents in living mice *Nat. Nanotechnol* **3** 557–62

Deurloo E E, Tanis P J, Gilhuijs K G A, Muller S H, Kroger R, Peterse J L, Rutgers E J T, Olmos R V and Kool L J S 2003 Reduction in the number of sentinel lymph node procedures by preoperative ultrasonography of the axilla in breast cancer *Eur. J. Cancer* **39** 1068–73

Dresselhaus M S, Dresselhaus G, Saito R and Jorio A 2005 Raman spectroscopy of carbon nanotubes *Phys. Rep.—Rev. Section of Phys. Lett.* **409** 47–99

Fu Q, Huang S M and Liu J 2004 Chemical vapor depositions of single-walled carbon nanotubes catalyzed by uniform $Fe_2O_3$ nanoclusters synthesized using diblock copolymer micelles *J. Phys. Chem.* B **108** 6124–9

Hoelen C G A, De Mul F F M, Pongers R and Dekker A 1998 Three-dimensional photoacoustic imaging of blood vessels in tissue *Opt. Lett.* **23** 648–50

Hughes M E, Brandin E and Golovchenko J A 2007 Optical absorption of DNA-carbon nanotube structures *Nano Lett.* **7** 1191–4

Krag D *et al* 1998 The sentinel node in breast cancer—a multicenter validation study *N. Engl. J. Med.* **339** 941–6

Krishnamurthy S, Sneige N, Bedi D G, Edieken B S, Fornage B D, Kuerer H M, Singletary S E and Hunt K K 2002 Role of ultrasound-guided fine-needle aspiration of indeterminate and suspicious axillary lymph nodes in the initial staging of breast carcinoma *Cancer* **95** 982–8

Ku G and Wang L H V 2005 Deeply penetrating photoacoustic tomography in biological tissues enhanced with an optical contrast agent *Opt. Lett.* **30** 507–9

Ku G, Wang X D, Xie X Y, Stoica G and Wang L H V 2005 Imaging of tumor angiogenesis in rat brains *in vivo* by photoacoustic tomography *Appl. Opt.* **44** 770–5

Margenthaler J A 2007 Depth measurement of sentinel lymph nodes in human, unpublished data

Maslov K, Stoica G and Wang L V H 2005 *In vivo* dark-field reflection-mode photoacoustic microscopy *Opt. Lett.* **30** 625–7

McMasters K M *et al* 2000 Sentinel lymph node biopsy for breast cancer: a suitable alternative to routine axillary dissection in multi-institutional practice when optimal technique is used *J. Clin. Oncol.* **18** 2560–6

NIH Consensus Statement 1990 Treatment of early stage breast cancer *NIH Consens. Statement* **8** 1–19

Pramanik M, Swierczewska M, Green D, Sitharaman B and Wang L H V 2009 Single-walled carbon nanotubes as a multimodal—thermoacoustic and photoacoustic—contrast agent *J. Biomed. Opt.* at press

Purushotham A D, Upponi S, Klevesath M B, Bobrow L, Millar K, Myles J P and Duffy S W 2005 Morbidity after sentinel lymph node biopsy in primary breast cancer: results from a randomized controlled trial *J. Clin. Oncol.* **23** 4312–21

Song K H, Stein E W, Margenthaler J A and Wang L H V 2008 Noninvasive photoacoustic identification of sentinel lymph nodes containing methylene blue *in vivo* in a rat model *J. Biomed. Opt.* **13** 054033

Song K H and Wang L H V 2007 Deep reflection-mode photoacoustic imaging of biological tissue *J. Biomed. Opt.* **12** 060503

Swenson K K, Nissen M J, Ceronsky C, Swenson L, Lee M W and Tuttle T M 2002 Comparison of side effects between sentinel lymph node and axillary lymph node dissection for breast cancer *Ann. Surg. Oncol.* **9** 745–53

Ung O A 2004 Australasian experience and trials in sentinel lymph node biopsy: the RACS SNAC trial *Asian J. Surg.* **27** 284–90

Wang X D, Pang Y J, Ku G, Xie X Y, Stoica G and Wang L H V 2003 Noninvasive laser-induced photoacoustic tomography for structural and functional *in vivo* imaging of the brain *Nat. Biotechnol.* **21** 803–6

Yamamoto K, Kamimura T and Matsumoto K 2005 Nitrogen doping of single-walled carbon nanotube by using mass-separated low-energy ion beams *Japan. J. Appl. Phys.* **1 44** 1611–4

Yang D W, Xing D, Gu H M, Tan Y and Zeng L M 2005 Fast multielement phase-controlled photoacoustic imaging based on limited-field-filtered back-projection algorithm *Appl. Phys. Lett.* **87** 194101

Yin B Z, Xing D, Wang Y, Zeng Y G, Zeng Y G, Tan Y and Chen Q 2004 Fast photoacoustic imaging system based on 320-element linear transducer array *Phys. Med. Biol.* **49** 1339–46

Zeng Y G, Xing D, Wang Y, Yin B Z and Chen Q 2004 Photoacoustic and ultrasonic coimage with a linear transducer array *Opt. Lett.* **29** 1760–2

Zhang H F, Maslov K, Stoica G and Wang L H V 2006 Functional photoacoustic microscopy for high-resolution and noninvasive *in vivo* imaging *Nat. Biotechnol.* **24** 848–51